

Power balance in highly loaded fluorescent lamps

G G Lister¹, J J Curry² and J E Lawler³

¹ Osram Sylvania, 71 Cherry Hill Drive, Beverly, MA 01915, USA

² National Institute of Standards and Technology, 100 Bureau Drive, Gaithersburg, MD 20899-8422, USA

³ Department of Physics, University of Wisconsin, 1150 University Avenue, Madison, WI 53706, USA

Received 29 June 2004, in final form 31 August 2004

Published 28 October 2004

Online at stacks.iop.org/JPhysD/37/3099

doi:10.1088/0022-3727/37/22/007

Abstract

Discrepancies reported in the literature between numerical predictions and experimental measurements in low-pressure Hg discharges at high current densities are considered. Elements of a one-dimensional fluid model and recent spectroscopic and Langmuir probe measurements are combined in a semi-empirical way to individually examine components of the positive column power balance and the discharge conductivity. At a Hg vapour pressure of 0.81 Pa (6.1 mTorr) and a current density of 300 mA cm^{-2} , previous discrepancies in the power balance and discharge conductivity are simultaneously resolved by assuming a higher electron density than that obtained from the Langmuir probe measurements. This conclusion is supported by independent measurements of ion density reported in a companion paper. The importance of radial cataphoresis under these conditions, particularly with regard to radiation transport, is highlighted. This work is of particular interest for the design of fluorescent lamps operating at high current densities.

(Some figures in this article are in colour only in the electronic version)

1. Introduction

The development of electrodeless lamps over the past decade—in which power is inductively coupled to the discharge by means of an external coil carrying a high-frequency electric current—has led to products such as Osram Sylvania's toroidal electrodeless lamp (ICETRON[®]) and the Philips⁴ (QL[®]). These lamps are members of a family of fluorescent lamps often referred to as highly loaded fluorescent lamps, that operate at current densities many times greater than in standard fluorescent lamps; other examples are compact fluorescent lamps and narrow-bore fluorescent lamps used for back-lighting. The results of experimental studies of these lamps [1–4] have been difficult to reconcile with predictions from numerical models [4–7].

⁴ Identification of commercial products in this paper is done solely for the purpose of clarity. Such identification neither implies recommendation or endorsement by the National Institute of Standards and Technology, nor does it imply that the equipment identified is necessarily the best available for the purpose.

Fluorescent lamps are low-pressure discharges containing argon or other rare gas at a few hundred Pascal (few Torr) and mercury of a few hundred milliPascal (few milliTorr). Self-consistent numerical models of these lamps under standard operating conditions (400 mA discharge current or 0.035 A cm^{-2} , 0.8 Pa (6 mTorr) Hg, 400 Pa (3 Torr) Ar) have reproduced experimental measurements reasonably well [8–12]. However, Langmuir probe measurements of electron densities [3, 7] and absorption spectroscopy measurements of mercury excited level densities [4] in highly loaded lamps show considerable disagreement with values predicted by the self-consistent models. Further, the measured electron densities are inconsistent with the calculated electrical conductivity necessary to describe the electrical characteristics of these lamps [5, 6].

In order to examine some of these discrepancies in more detail, we have performed a power balance analysis of a highly loaded fluorescent lamp, based on experimental measurements of electron and excited level densities and electron temperature.

In standard models of the positive column [7–12] the power balance is self-consistently calculated from the rate coefficients for all atomic processes in the plasma. This approach relies on a detailed knowledge of the cross sections for these processes, many of which remain ill defined. Our approach, which is semi-empirical, allows us to interpret the experimental data in such a way as to quantitatively apportion the power dissipated in the discharge.

The various components contributing to the power dissipation in the positive column are discussed in section 2. Section 3 describes the experimental lamp studied. A one-dimensional fluid model used in the power balance is described in section 4. Section 5 contains a power balance analysis, based on the experimental measurements and elements of the model. A discussion of the implications of these results is presented in section 6. Our conclusions are summarized in section 7.

2. Power balance in the positive column

In this analysis we are focusing on the power flow at the wall, which must precisely balance the electrical input power during steady-state operation. Dissipation of electrical power in the positive column of a fluorescent lamp can be partitioned into three channels:

- (i) escape of radiation to the wall,
- (ii) volume losses, i.e. heating of gas atoms by elastic collisions with charged particles, followed by thermal conduction to the wall, and
- (iii) other (electronic) wall losses, i.e. quenching of metastable atoms and recombination of ions and electrons at the discharge wall.

Fluorescent lamps are optimized to maximize the power dissipated as ultraviolet (UV) radiation at 254 nm, reaching as much as 60% of the electrical input power in the positive column. UV photons produced in the discharge undergo frequent absorption and re-emission cycles during their escape to the wall. Theoretical and experimental analysis of radiation trapping is therefore vital to understanding the power balance in the discharge.

In standard fluorescent lamp discharges, the rare gas pressure is 400–700 Pa (3–5 Torr) and volume losses due to gas heating represent the most important mechanism for power dissipation after radiation [13]. In electrodeless lamps, however, rare gas pressures of a few tens of Pascals (few hundred milliTorr) are common and wall losses are typically greater than volume losses.

Higher currents and lower gas filling pressures in electrodeless lamps imply that Coulomb collisions between electrons and ions are much more important in limiting the electrical conductivity than in standard fluorescent lamps. Electron–electron Coulomb scattering has no effect on the conductivity, since such collisions do not change the momentum of the electron gas. In the discharge considered in this paper, values of n_e/N , the ratio of electron to gas density, are typically $(1–5) \times 10^{-4}$. For these ratios, electron–electron collisions are insignificant in establishing the high-energy tail of the electron energy distribution function (EEDF). However, the cross sections for electron–ion Coulomb cross sections below 1 eV are many orders of magnitude higher than the

electron–neutral atom momentum transfer cross sections and are very important in limiting the electrical conductivity, particularly for electron energies close to the Ramsauer minimum of argon. The influence of Coulomb collisions on electrical conductivity will be quantitatively discussed in section 4.1.

Mercury depletion in the central region of the positive column due to *radial cataphoresis* can be especially important in highly loaded fluorescent lamps. Cataphoresis, or the partial segregation of gas components in an electrical discharge, is a well-known and well-studied phenomenon [14]. It occurs as the result of the greatly different speeds with which neutral atoms and ions diffuse through the buffer gas. Hg ions, accelerated in the radial ambipolar electric field, diffuse to the wall much more quickly than Hg atoms, formed by recombination of ions at the wall, can diffuse back to the centre. This leads to axial depletion of Hg atoms, which influences the power balance in several ways:

- (i) it modifies the electrical conductivity of the discharge, and
- (ii) it reduces the radiation trapping by reducing the total number of absorbing Hg atoms and by broadening the spatial distribution of excited Hg atoms.

When radial cataphoresis is severe,

- (iii) it influences the spatial profile of the production rate of atomic mercury ions, and
- (iv) it reduces the average ambipolar diffusion time through excitation of higher-order diffusion modes.

Recent experiments performed to measure cataphoresis in a discharge similar to the one discussed here are reported in a companion paper [15] and the importance of cataphoresis to the power balance in highly loaded fluorescent lamps is discussed in section 5.1.

3. The highly loaded discharge lamp

The design of the discharge used in the experiments was described in [4] and is illustrated in figure 1. The lamp forms a closed tubular loop that passes through two toroidal ferrite cores, each wound with an induction coil, so that the voltage in the lamp is induced by a magnetic field contained entirely within the ferrite cores. The lamp is 35 cm long,

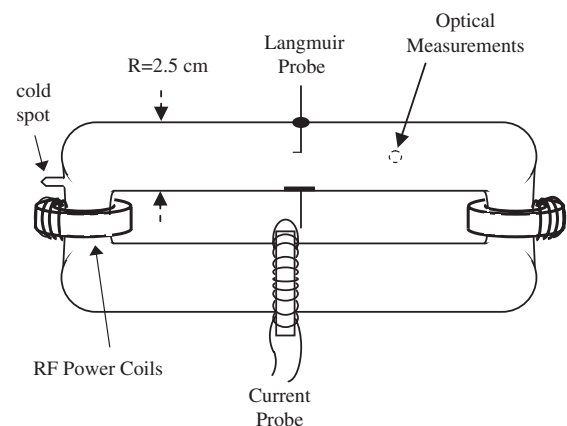


Figure 1. Schematic drawing of the highly loaded closed-loop discharge lamp.

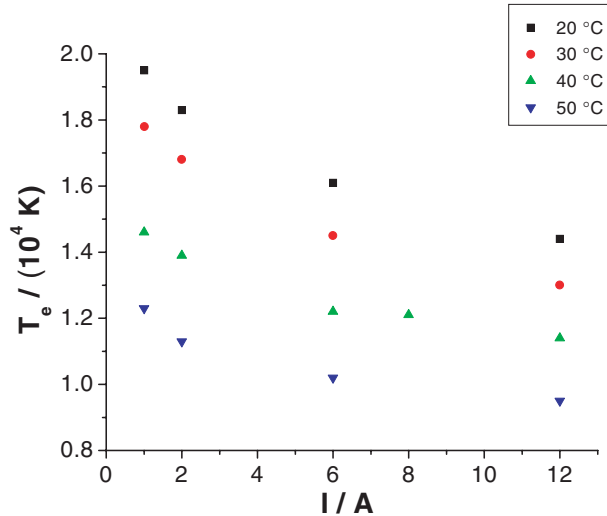


Figure 2. Langmuir probe measurements of electron temperature as a function of discharge current and cold spot temperature.

with a discharge path of 75 cm, and operates at a frequency of 250 kHz. The design of the lamp is modelled on Osram Sylvania's toroidal electrodeless lamp (ICETRON®).

The discharge current was measured with a calibrated current transformer and the discharge voltage around the loop was measured by a high-impedance pick-up loop running parallel to the discharge.

The lamp is filled with argon at 40 Pa (300 mTorr) at 20°C. A small stem constitutes the cold spot on the discharge cell, and its temperature was stabilized thermo-electrically to set and maintain a fixed vapour pressure. The discharge tube is fitted with a Langmuir probe at the centre of one of the straight arms.

Three different types of data have been previously measured in this system over a wide range of currents and mercury vapour pressures:

- (i) discharge current and axial electric field [3, 4],
- (ii) EEDF on-axis [3], used to infer the electron density and temperature, and
- (iii) Hg $6p^3P_{0,1,2}$ and $6p^1P_1$ excited level column densities across the tube, $\overline{NL} = 2 \int_0^R n_x(r) dr$ [4].

Data exist for discharge currents over the range 1–12 A and for Hg vapour pressures of 0.16 Pa (1.2 mTorr), 0.37 Pa (2.8 mTorr), 0.81 Pa (6.1 mTorr), and 1.7 Pa (13 mTorr). These vapour pressures correspond to cold spot temperatures of 20°C, 30°C, 40°C, and 50°C, respectively. The previously reported Langmuir probe measurements of electron densities and temperatures [3] are reproduced in figures 2 and 3.

Measurements of the $6p^3P_1$ and $6p^1P_1$ column densities are discussed in [4]. The experimental data are combined with elements of a one-dimensional fluid model described below to semi-empirically calculate the power balance in the discharge.

4. One-dimensional fluid model

The difficulty in reconciling experimental measurements in highly loaded Hg discharges with self-consistent numerical models has been well documented elsewhere [4–6]. In an

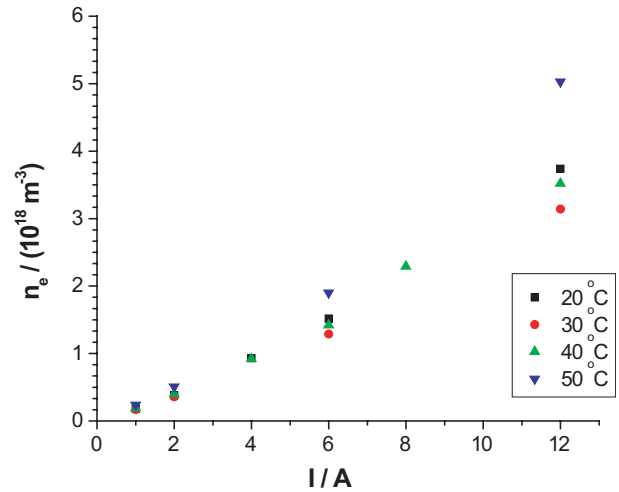


Figure 3. Langmuir probe measurements of electron density as a function of discharge current and cold spot temperature.

attempt to explain some of these differences, we have used elements of a one-dimensional fluid model, based on the experimental measurements, to provide a detailed power balance analysis of the discharge, similar to that conducted on standard fluorescent lamps [13, 16]. The model is not being used here for a complete, *a priori* discharge simulation. Measured electron densities, electron temperatures, and excited level column densities are substituted into equations from the model in order to evaluate pieces of the power balance.

The total electrical power per unit length, W , dissipated in the positive column of a fluorescent lamp is the product of the discharge current, I , and the electric field, E_z , and can be written as

$$W = IE_z = W_{\text{rad}} + W_{\text{heat}} + W_{\text{wall}}, \quad (1)$$

where W_{rad} , W_{heat} , and W_{wall} are the power dissipation per unit length due to radiation, gas heating, and electronic wall losses, respectively. These electronic wall losses include all non-radiative inelastic losses involving electrons and neutral atoms. Metastable atoms and ions are assumed to diffuse to the wall, where the metastable atoms release their excess energy and the ions recombine with electrons.

In order to incorporate the available experimental measurements into elements of the model described below, it is necessary to make some assumptions about the shape of radial density profiles for both electrons and excited level densities. In the calculations described in section 5, the electron and mercury metastable density profiles are assumed to be zero-order Bessel functions, $n_j(r) = n_j(0)J_0(kr)$. Here $kR = 2.405$ is the first zero of the Bessel function at $r = R$, the discharge radius. Experimental measurements in standard fluorescent lamps [16] have shown that this is a good approximation for electron density. For radial profiles of mercury atoms in the $6p^3P_1$ and $6p^1P_1$ resonance levels we used fundamental mode solutions to the Holstein–Biberman radiation transport equation (section 4.3). The influence of the density profiles on the results is discussed in section 6.

4.1. Electrical characteristics and Ohm's Law

The discharge current, I , and axial electric field, E_z , are related through the electrical conductivity of the plasma, σ_e ,

$$I = 2\pi E_z \int_0^R \sigma_e(r) r dr, \quad (2)$$

where

$$\sigma_e = -\frac{n_e}{3N} \left(\frac{2e}{m_e}\right)^{1/2} \int_0^\infty \frac{\varepsilon}{q_t(\varepsilon)} \frac{\partial f_0}{\partial \varepsilon} d\varepsilon, \quad (3)$$

n_e is the electron density, N is the total gas density, $f_0(\varepsilon)$ is the isotropic component of the electron energy *probability* function for electron energy, ε , $\int_0^\infty \varepsilon^{1/2} f_0(\varepsilon) d\varepsilon = 1$,

$$q_t(\varepsilon) = q_{em}(\varepsilon) + q_{inel}(\varepsilon) + \frac{n_e}{N} \frac{q_e(\varepsilon)}{\gamma_E} \quad (4)$$

is the total electron transport cross section [10], where $q_{em}(\varepsilon)$ is the total elastic momentum transfer cross section, $q_{inel}(\varepsilon)$ is the total inelastic cross section, $q_e(\varepsilon)$ is the electron-ion Coulomb cross section in a Lorentz gas [17],

$$q_e(\varepsilon) = \frac{\pi}{\varepsilon^2} \left(\frac{e^2}{4\pi\varepsilon_0}\right)^2 \ln \Lambda, \\ \ln \Lambda = \frac{1}{2} \ln \left(\frac{n_e e^6}{9(4\pi)^2 (\varepsilon_0 k \varepsilon_e)^3}\right) \quad (5)$$

and γ_E is a correction factor to allow for the effect of electron-electron interactions. For a singly ionized gas $\gamma_E = 0.582$ [18].

Electron-ion Coulomb collisions are important in these discharges for low electron energies, because of the $1/\varepsilon^2$ dependence of the cross section. For electrons with energy 1 eV in an Hg-Ar discharge of electron temperature 1 eV, $q_e \approx 7.3 \times 10^{-17} \text{ m}^2$ and the elastic momentum transfer for argon $q_{Ar} \approx 10^{-20} \text{ m}^2$. Under these conditions and with typical values of $n_e/N \sim 10^{-4}$, the rate of momentum transfer due to electron-ion collisions is of the same order as the rate for electron-Ar atom collisions. The electron-ion mechanism is even more important for average electron energies at the Ramsauer minimum for argon, 0.3 eV, where $q_{Ar} \approx 1.5 \times 10^{-21} \text{ m}^2$. Here the Coulomb term dominates.

The Langmuir probe measurements of electron density and temperature [3], together with the recommended electron-momentum cross sections for Hg and Ar, have been used to calculate the electrical conductivity [5, 6]. It was shown that if these calculated values of σ_e and the measured electric field are substituted in equation (2), the calculated discharge current is a factor of 2 smaller than that measured experimentally. A similar discrepancy was found for standard fluorescent lamps, particularly at higher currents [7]. The good agreement between earlier models [9, 11, 12] and experimental measurements for these lamps is due in part to their neglect of electron-ion Coulomb collisions, which become increasingly important as current density increases.

4.2. Radial cataphoresis and gas heating

If ionization of argon and the diffusion of excited state atoms are neglected, the outward radial flux of charged particles,

electrons, and mercury ions balances the influx of ground state mercury atoms, and

$$D_{\text{Hg}} N \frac{d}{dr} \left(\frac{n_{\text{Hg}}}{N}\right) = -D_a \frac{dn_e}{dr}, \quad (6)$$

where D_{Hg} and n_{Hg} are the diffusion coefficient and density for ground state mercury atoms, D_a is the ambipolar diffusion coefficient, and n_e is the electron density. Since metastable densities in fluorescent lamps represent only about 1% of the ground state density, their contribution to equation (6) is negligible. In the case of strong cataphoresis, the contribution of argon ions might be considerable and their neglect is not justified.

If gas heating is small, $D_a/D_{\text{Hg}} \sim T_e/T_g \gg 1$, where T_e and T_g are the electron and gas temperatures and the difference between the axial and wall densities of ground state mercury is $\Delta n_{\text{Hg}} \sim (T_e/T_g) n_e(0)$. The fractional depletion of mercury atoms on-axis therefore increases with increasing electron density or decreasing mercury vapour pressure (cold spot temperature).

The total gas density, N , is a function of the gas temperature, which may be estimated using the heat conduction equation,

$$\frac{1}{r} \frac{d}{dr} \left(\kappa_g r \frac{dT_g}{dr}\right) + H_{\text{el}}(r) = 0, \quad (7)$$

where κ_g is the thermal conductivity of the gas and

$$H_{\text{el}}(r) = 2\sqrt{2} m_e^{1/2} n_e \int_0^\infty \sum_s \frac{N_s}{M_s} q_{em}^s(\varepsilon) \left(\varepsilon - \frac{3k_B T_g}{2}\right) \varepsilon \\ \times f(\varepsilon) d\varepsilon + e n_e \mu_i E_r^2. \quad (8)$$

Here M_s and N_s are the atomic mass and gas density, respectively, for species s and $E_r = -(k_B T_e / e n_e) (dn_e / dr)$ is the ambipolar electric field. The first term in the rhs of equation (8) represents the gas heating by electron-atom collisions [19, 20], while the second term is due to ion-atom collisions. The total power dissipated by gas heating is then

$$W_{\text{heat}} = 2\pi \int_0^R H_{\text{el}}(r) r dr. \quad (9)$$

4.3. Radiation

The total power per unit length escaping from the discharge in the radiative transition $j \rightarrow k$ is

$$W_{\text{rad}}(\lambda_{jk}) = 2\pi \varepsilon_{jk} \beta_{jk} \int_0^R n_j(r) r dr, \quad (10)$$

where λ_{jk} is the radiated wavelength for the transition, β_{jk} is the trapped decay rate associated with the fundamental mode, and ε_{jk} is the energy difference between the excited levels.

Values of β_{jk} for 254 nm radiation as a function of ground state mercury density, n_{Hg} , gas temperature, T_g , and the discharge radius, R , were calculated using a general analytic formula developed by Lawler and Curry [21], which is applicable to single-component line shapes dominated by any combination of radiative, Doppler, and resonance collisional broadening. This formula was later extended to include the

influences of foreign gas broadening [22] as well as non-uniform distributions of ground state atoms such as those resulting from radial cataphoresis [23]. Since this formula is valid only for a single-component line shape, the hyperfine structure of the Hg 254 nm line was taken into account by assuming a factor of 5 reduction in the absorbing atom density. This approximates the hyperfine and isotopic structure of the Hg 254 nm line as five well-separated components with equal magnitudes [24]. We tested the accuracy of this approximation for the case of a uniformly distributed Hg ground state density using Monte Carlo simulations of radiation transport of the kind described in [25]. The difference between the single-component approximation and a calculation with the full hyperfine and isotopic structure is approximately 30% for a Hg vapour pressure of 0.16 Pa (20°C). However, the difference decreases rapidly with increasing Hg density, so that for a Hg vapour pressure of 0.81 Pa (40°C) and 1.7 Pa (50°C), the differences are negligible.

The treatment of partial frequency redistribution and the isotopic structure in radiation transport simulations for the Hg 185 nm line is more complex than that for the 254 nm line, and a special formula, applicable only to the 185 nm line, was developed from experimental measurements and Monte Carlo simulations [25].

In order to use equation (10) to calculate the power dissipated as radiation in the discharge, we require a relationship between the experimentally measured resonance level column densities $\overline{NL} = 2 \int_0^R n_j(r) dr$ and the total number of resonance level mercury atoms per unit length in the discharge $N_T = 2\pi \int_0^R n_j(r) r dr$. Profiles of $n_j(r)$ have been obtained from numerical solutions to the Holstein–Biberman radiation transport equation [23] for the case of the 6p 3P_1 level using a Doppler-broadened line shape with the factor of 5 assumption discussed above to account for the hyperfine and isotopic structure of the 254 nm line. The model also includes the calculated depletion of the Hg ground level due to radial cataphoresis. The radial profile for the 6p 1P_1 level was assumed to be the same as for the 6p 3P_1 level. Results of these radiation transport simulations can be expressed in terms of the quantity F_j , where

$$F_j = \frac{N_T}{1.21 R \overline{NL}}. \quad (11)$$

Therefore, equation (10) can be rewritten as

$$W_{\text{rad}}(\lambda_{jk}) = 1.21 F_j \varepsilon_{jk} \beta_{jk} R \overline{NL}. \quad (12)$$

It should be noted that $F_j = 1$ if the fundamental mode is not affected by radial cataphoresis; thus F is a measure of the broadening of the fundamental mode from radial cataphoresis. The numerical factor of 1.21 in the definition of F is evaluated from the known analytic solution to the Holstein–Biberman equation with a Doppler-broadened line shape, e.g. van Trigt's [26] solution, in which the fundamental mode is expressed as a sum of Jacobi polynomials. If the actual resonance level profiles are broader than the fundamental mode solution, this will increase F_j (equation (12)) and consequently increase the power dissipated as radiation.

4.4. Electronic wall losses

Losses to the wall are the sum of diffusion of metastable atoms and ions to the wall,

$$W_{\text{wall}} = W_{\text{meta}} + W_{\text{ion}}. \quad (13)$$

Metastable diffusion. The power dissipation per unit length in the positive column due to metastable atom diffusion to the wall, W_{meta} , is

$$W_{\text{meta}} = 2\pi R \sum_j \varepsilon_j \Gamma_j(R), \quad (14)$$

where ε_j is the excitation energy of the metastable level j and $\Gamma_j(R) = -D_j N(d/dr)(n_j/N)$ is the flux of metastable atoms to the wall.

Ionization. The power dissipation per unit length in the positive column due to charged particle diffusion to the wall, W_{ion} , is

$$W_{\text{ion}} = 2\pi R(\varepsilon_i + \varepsilon_{\text{ew}} + \varepsilon_{\text{iw}})\Gamma_i(R), \quad (15)$$

where ε_i is the ionization energy of the atom from the ground state, ε_{ew} and ε_{iw} are the average kinetic energy of electrons and ions striking the wall, and $\Gamma_i(R) = -D_a dn_i/dr$ is the ion flux to the wall. For a Maxwell–Boltzmann EEDF, $\varepsilon_{\text{ew}} = 2kT_e$ and

$$\varepsilon_{\text{iw}} = eV_w + \frac{1}{2}kT_e, \quad (16)$$

where $V_w = (kT_e/e) \ln(M_s/2\pi m_e)^{1/2}$ is the floating potential of the wall with respect to the sheath potential edge [27] and the second term in equation (16) represents the Bohm energy of ions entering the sheath.

5. Analysis of a highly loaded fluorescent lamp

5.1. Radial cataphoresis

The ratios of the mercury density on-axis to that at the wall obtained from the simplified model are plotted in figure 4. The mercury ground state density profiles were calculated from equations (6) and (7), using the axial electron densities and temperatures obtained from the Langmuir probe measurements and assuming $n_e(r) = n_e(0)J_0(2.405r/R)$. As expected, mercury depletion is greatest for high discharge currents and low cold spot temperatures. In fact, for currents above 6 A and cold spot temperature of 20°C, these estimates predict *negative* mercury densities on-axis. This unphysical result implies that there is strong ionization of argon atoms, which is not included in the model. Experiments to measure mercury depletion in a similar discharge at a cold spot temperature of 50°C and discharge currents from 4 to 8 A are reported on in a companion paper [15], and the results are in good agreement with these calculations.

The following discussion is limited to experiments at mercury vapour pressures of 0.81 Pa (6.1 mTorr), corresponding to a cold spot temperature of 40°C, and discharge currents up to 6 A, for which mercury depletion is predicted to be less than 20%.

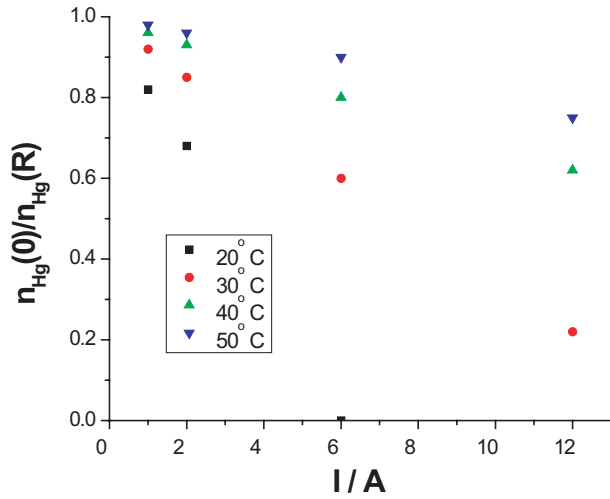


Figure 4. Ratio of calculated mercury ground state atom density on-axis to the density at the wall as a function of discharge current, for various cold spot temperatures.

Table 1. Power balance obtained using a one-dimensional fluid model, coupled with experimental measurements of electron density, electron temperature, and Hg $6p^3P_{0,1,2}$ and $6p^1P_1$ densities.

	I/A		
	2	4	6
F_{254}	1.02	1.06	1.09
E_z ($V\ m^{-1}$)	45.3	41.1	34.2
W_{254} ($W\ m^{-1}$)	40.8	55.2	59.5
W_{185}	16.1	30.5	28.5
W_{vis}	2.7	6.5	5.5
W_{heat}	4.5	9.1	11.4
W_{wall}	5.1	10.9	14.8
$W_{calc} = W_{rad} + W_{heat} + W_{wall}$	69.2	112.3	119.7
$W_{meas} = IE_z$	90.6	164.4	205.2

5.2. Power balance

The power balance in the discharge at 40°C cold spot temperature as a function of discharge current, calculated from measured quantities using the analysis described earlier, is illustrated in table 1. Values of F_{254} were obtained from simulations of the fundamental mode for radiation transport, including the cataphoresis calculated from the Langmuir probe measurements, and these F values were also applied to the W_{185} calculations.

There is clearly a large shortfall in the sum of the calculated power dissipated by the sum of radiation, gas heating, and electronic wall losses, W_{calc} , compared with the known electrical power in the discharge, W_{meas} .

6. Discussion

6.1. Ohm's Law

The discrepancies between the calculated and measured discharge currents discussed in section 4.1 are fundamental to the interpretation of the experimental data for apportioning the power dissipation mechanisms in the discharge. The current and the electric field can be measured within a few per cent. Langmuir probe measurements of the electron temperature

below the first excitation energy of mercury are less subject to errors than measurements of the electron density. Further, electrical conductivity is relatively insensitive to electron temperature—a change of 1000 K results in a 10% change in electrical conductivity. This implies that the Langmuir probe measurements of electron density are too low, or the two-term Boltzmann expansion to derive the electrical conductivity is not applicable to highly loaded lamps, or the cross sections are not sufficiently accurate.

Measurements of electron densities in pure mercury and pure argon positive column discharges using a microwave interferometer [28] have obtained values that are consistent with Ohm's Law and considerably higher than those obtained from Langmuir probe measurements made in the same discharge. Independent measurements of ion densities in a similar discharge, using a synchrotron radiation absorption experiment and confirmed by microwave interferometer experiments, are presented in a companion paper [15]. These measurements are also considerably higher than those obtained using the Langmuir probe. Note that if the actual electron density is higher than that measured by the Langmuir probes, cataphoresis would be even more severe.

6.2. UV radiation

The power dissipated as UV radiation for a 2 A discharge current (table 1), calculated from the resonance level density measurements, is $56.9\ W\ m^{-1}$, representing 63% of the total electrical power in the discharge. This percentage is comparable with that measured in standard fluorescent lamps [13]. However, for a lamp discharge current of 6 A, the percentage of electrical power converted to UV radiation is calculated to be 43%, significantly lower than the known performance of ICETRON® lamps.

An alternative estimate of the total UV radiated power from an ICETRON® lamp has been obtained by analysing spectral output measurements made in an integrating sphere on 100 W ICETRON® lamps with and without a phosphor coating and run on 100 W and 150 W ballasts, corresponding to discharge currents of approximately 4 A and 6 A, respectively. An integrating sphere is a low-spectral resolution, absolutely calibrated, spatially averaged emission spectroscopy measurement. Integrating spheres and standard lamps with known power output per spectral interval are highly developed for this region. The measurements are performed by completely enclosing the lamp in the sphere, and detectors, usually with appropriate filtering, are calibrated to measure the total power, $W_{rad}(\lambda_j)$, emitted by a spectral line (from the discharge or by a phosphor band) between the wavelengths λ_j and $\lambda_j + \Delta\lambda$. The total number per unit time of photons emitted from the lamp is then

$$N_v = \sum_j \frac{\lambda_j W(\lambda_j)}{hc}, \quad (17)$$

where the summation is over visible wavelengths. Denoting the number per unit time of visible photons emitted from the phosphor coated and uncoated lamps by N_{phos} and N_{vis} , respectively, and assuming that the quantum efficiency of converting UV photons to photons in the visible spectrum

Table 2. Power balance in a highly loaded Hg discharge based on radiometric measurements of UV and visible radiation from an ICETRON® lamp. The values of W_{UV} in parentheses, gas heating, W_{heat} , and wall losses, W_{wall} , were obtained assuming the electron density calculated from equation (2) and, in the case of W_{UV} , the measured resonance level densities.

	I/A	
	4	6
F_{254}	1.09	1.21
W_{UV} ($W m^{-1}$)	98.6 (90.0)	118.3 (114.8)
W_{vis}	8.3	11.8
W_{heat}	15.5	23.0
W_{wall}	18.8	29.6
$W_{calc} = W_{rad} + W_{heat} + W_{wall}$	141.2 (132.6)	182.7 (179.2)
W_{meas}	155.0	205.0

is 0.9, the total number per unit time of UV photons emitted by the discharge is $N_{UV} = (N_{phos} - N_{vis})/0.9$.

In order to estimate the total UV radiative power emitted by the discharge, it is necessary to make an assumption about the fractions emitted at 185 nm and 254 nm, respectively. If we assume that the ratio is that calculated from the results of table 1, then the total UV power per unit length emitted by the discharge is found to be $98.6 W m^{-1}$ and $118.3 W m^{-1}$ for discharge currents of 4 A and 6 A, respectively (table 2). This means that the fractions of electrical power converted to UV radiation are 63% and 57%, respectively, in line with the observed performance of ICETRON® lamps.

6.3. Power balance with a higher electron density

If the Langmuir probe data seriously underestimate the electron density on the axis of the discharge, as suggested by the results of independent measurements [15, 28], then power dissipated in gas heating, wall losses, and radiation will all be underestimated as well. Our calculation of UV output is significantly affected by our calculation of radial cataphoresis based on the measured electron density. The effect of higher mercury depletion on-axis will result in reduced radiation trapping and a higher calculated UV output.

In order to demonstrate the importance of the electron density measurements on the power balance analysis of the discharge, we have recalculated the gas heating and wall losses, assuming the electron density is that required to satisfy Ohm's Law in equation (2). The resulting power balance (table 2), including the UV and visible radiation obtained from the integrating sphere measurements, is now in good agreement with the measured electrical power in the discharge, the shortfall in accounted power now being $\sim 10\%$, which is within the accuracy of the model described here.

The cataphoresis and radiation transport were also recalculated using the adjusted values of electron density, and the new values of F_{254} are shown in table 2. If these values are then included in equation (13), the calculated UV radiation is within 10% of the value deduced from the integrating sphere measurements. This suggests that previous discrepancies may be largely explained by the change in radiation transport due to cataphoresis. The remaining discrepancy may be accounted for by deviations from the assumed Bessel function for the electron density profile in the radiation transport

programme. Ion density profiles reported in the companion paper [15] indicate significant deviations from the zeroth-order Bessel function approximation for the radial electron density distribution.

7. Conclusions

Analysis of a highly loaded Hg discharge using elements of a one-dimensional fluid model, together with the results of experimental measurements of the resonance level densities of mercury atoms at high discharge currents shows considerable discrepancies with measurements of the total radiation output of these lamps under highly loaded conditions. These discrepancies can be explained by correctly accounting for radial cataphoresis of Hg atoms in simulations of radiation transport.

Earlier papers [5–7] have brought into question the validity of Langmuir probe measurements in measuring the electron density in the positive column of mercury rare gas discharges, and there is substantial evidence that these measurements are in error by as much as a factor of 2 in highly loaded lamps. Independent measurements reported in a companion paper [15] support this conclusion. If electron densities corresponding to those required to satisfy Ohm's Law are used to estimate the power dissipation due to gas heating and wall losses, and the measured total radiation output is included in the power balance analysis, the power balance in these lamps can be completed within about 10%. This is well within the accuracy of the model adopted and is similar to the results obtained from the power balance of standard fluorescent lamps by Koedam *et al* [13].

It was noted in [4] that the discrepancies between measured and calculated mercury excited level densities from a self-consistent model indicate that important mechanisms for depopulating these levels and enhancing the ionization balance are missing from the models. There is clearly a need to better understand the role of multi-step ionization, identified as an important process by Wani [29]. The application of advanced computer programs to calculate many of the unknown electron impact cross sections should help to resolve this issue.

Acknowledgments

This work was supported by the EPRI/ALITE Consortium, Osram Sylvania, and the National Science Foundation. We are grateful to R Piejak for kindly allowing us to reproduce the Langmuir probe measurements and K Phan for the spectral data obtained from integrating sphere experiments.

References

- [1] Jonkers J, Bakker M and van der Mullen J A M 1997 *J. Phys. D: Appl. Phys.* **30** 1928
- [2] Jonkers J, van Dijk J and van der Mullen J A M 1999 *J. Phys. D: Appl. Phys.* **32** 898
- [3] Godyak V A, Piejak R A and Alexandrovich B M 2001 *Symp. Proc.: The 9th Int. Symp. on the Science and Technology of Light Sources* (Ithaca, NY: Cornell Print and Digital Copy Services) p 157
- [4] Curry J J, Lister G G and Lawler J E 2002 *J. Phys. D: Appl. Phys.* **35** 2945

-
- [5] Lister G G 1999 *Advanced Technologies Based on Wave and Beam Generated Plasmas* ed H Schlüter and A Shivarova (Dordrecht: Kluwer) p 65
- [6] Lister G G 2003 *Phys. Plasmas* **10** 2136
- [7] Kreher J and Stern W 1988 *Contrib. Plasma Phys.* **28** 185
Kreher J and Stern W 1989 *Contrib. Plasma Phys.* **29** 181
- [8] Winkler R B, Wilhelm J and Winkler R 1983 *Ann. Phys.* **40** 90
Winkler R B, Wilhelm J and Winkler R 1983 *Ann. Phys.* **40** 119
- [9] Dakin J T 1986 *J. Appl. Phys.* **60** 563
- [10] Maya J and Lagushenko R 1989 *Adv. Atom. Mol. Optic. Phys.* **26** 321
- [11] Zissis G, Bénétruy P and Bernat I 1992 *Phys. Rev. A* **45** 1135
- [12] Lister G G and Coe S E 1993 *Comput. Phys. Commun.* **75** 160
- [13] Koedam M, Kruithof A A and Riemens J 1963 *Physica* **29** 565
- [14] Chanin L M 1978 *Gaseous Electronics* vol 1 (New York: Academic) p 133
- [15] Aiura Y and Lawler J E 2004 submitted
- [16] Verweij W 1961 *Philips Res. Rep.* **2** (Suppl.) 1
- [17] Spitzer L 1961 *Physics of Fully Ionized Gases* 2 edn (New York: Interscience)
- [18] Spitzer L and Härm R 1953 *Phys. Rev.* **89** 977
- [19] Kenty C, Easley M A and Barnes B T 1951 *J. Appl. Phys.* **22** 1006
- [20] Lawler J E, Den Hartog E A and Hitchon W N G 1991 *Phys. Rev. A* **43** 4427
- [21] Lawler J E and Curry J J 1998 *J. Phys. D: Appl. Phys.* **31** 3235
- [22] Lawler J E, Curry J J and Lister G G 2000 *J. Phys. D: Appl. Phys.* **33** 252
- [23] Curry J J, Lawler J E and Lister G G 1999 *J. Appl. Phys.* **86** 731
- [24] Schweitzer W G 1963 *J. Opt. Soc. Am.* **53** 1055
- [25] Menningen K L and Lawler J E 2000 *J. Appl. Phys.* **88** 3190
- [26] van Trigt C 1976 *Phys. Rev. A* **13** 726
- [27] Lieberman M A and Lichtenberg A J 1994 *Principles of Plasma Discharges and Materials Processing* (New York: Wiley) p 161
- [28] Garner R 2004 private communication
- [29] Wani K 1994 *J. Appl. Phys.* **75** 4917